Experimental and Theoretical Study on the Nature of Adsorbed Oxygen Species on Shaped Ceria Nanoparticles

Christian Schilling[a], *M. Verónica Ganduglia-Pirovano**[b], *and Christian Hess**[a]

[a] Eduard-Zintl-Institut für Anorganische und Physikalische Chemie, Technische Universität Darmstadt, Alarich-Weiss-Str. 8, 64287 Darmstadt, Germany

[b] Instituto de Catálisis y Petroleoquímica, Consejo Superior de Investigaciones Científicas, Marie Curie 2, 28049, Madrid, Spain

Corresponding Author

* Christian Hess: hess@pc.chemie.tu-darmstadt.de,

* M. Verónica Ganduglia-Pirovano: vgp@icp.csic.es

Abstract

Ceria is widely used in heterogeneous catalysis owing to its redox properties. Engineering the shape of ceria particles offers a powerful tool to develop materials with enhanced catalytic properties. In this study, we provide evidence for the shape-dependent dioxygen adsorption and activation of ceria nanoparticles with (111) and (100) facets by in situ Raman spectroscopy and relate these properties to unique adsorption sites employing density functional theory. Temperature- and gas phase-dependent experiments demonstrate a facilitated formation of peroxide, superoxide, and weakly bound dioxygen species on the (100) facets as rationalized by calculated vibrational frequencies of O_2^{2-}, O_2^-, and O_2 species on CeO_{2-x}(100) surfaces. Our results show that the localization of the excess charge, driving the $Ce^{4+} \rightarrow Ce^{3+}$ reduction, significantly affects the stretching vibrations. Our approach provides a powerful basis for future developments of ceria based catalysts by bridging the materials gap between idealized and real catalytic systems.

TOC graphic

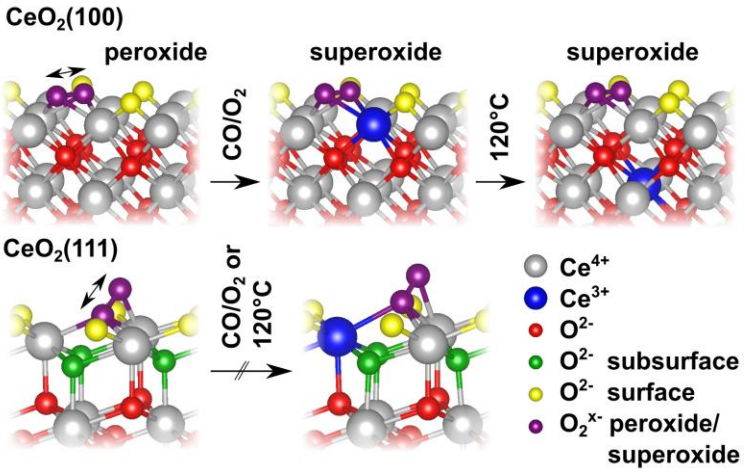

Ceria is an important metal oxide used as oxygen buffer material in automotive exhaust treatment, [1] [2] as a catalyst [3] [4] as well as non-innocent oxide support in catalysis,[5] [6] [7] in fuel-cell applications, [8] and as photo catalyst. [9] The morphology and size of ceria nanoparticles affect their performance in applications as the differently exposed facets are not equal with respect to the atomic arrangement. [10] In particular, studies on well-defined ceria nanocrystals have clearly established that the exposure of specific surface terminations affects the surface chemistry, [11] oxygen storage capacity [12] [13] and reactivity, [14] [15] providing a precious tool to enable the bridging of the materials gap between the knowledge from studies on planar surfaces [16] [17] [18] and that from powder samples, which are of relevance for catalysis. In this context, we highlight the relevance of shaped ceria nanoparticles for catalytic processes taking place at lower temperatures, i.e., oxidation of volatile organic compounds, [19] or CO oxidation and water-gas shift reaction in the presence of gold. [14] [5]

The ceria functionality in applications is strongly related to the ease with which oxygen vacancies can be created, which is accompanied by the localization of the excess charge on cerium ions. At these vacancy sites, molecular oxygen (O_2) can be activated via the formation of weakly adsorbed dioxygen ($O_{2,ads}^{\delta-}$), superoxide (O_2^-), and/or peroxide (O_2^{2-}) species according to the following reactions:

$$O_{2,gas} \rightarrow O_{2,ads}^{\delta-} \rightarrow O_2^- \rightarrow O_2^{2-} \rightarrow 2\,O_{lattice}^{2-}$$

Raman spectroscopy has previously been applied to polycrystalline ceria [20] [21] [22] [23] as well as ceria nanocubes, rods and polyhedra, [24] and both peroxide and superoxide species have generally been observed, although not for the case of the nanocubes for which superoxide species have not yet been reported. Further, IR spectroscopy has enabled the detection of superoxide species at

polycrystalline ceria surfaces [25] and ceria nanorods, [26 27] as well as peroxide and superoxide species at the crystalline CeO_2(110) surface, [16] and superoxide species at the CeO_2(100) surface; [16] however, no reactive dioxygen species were observed at the crystalline CeO_2(111) surface. [16] Despite these studies there is still no consistent picture of oxygen adsorption at shaped ceria nanoparticles in the literature, probably due to the presence of impurities resulting from the synthesis and/or size effects.

Density functional theory (DFT) with an on-site Coulomb correction (DFT+U) [28 29] has been employed to model the formation of superoxide and peroxide species on ceria surfaces. [18 30 31] In particular, at a surface defect on the (111) and (100) surfaces, the higher stability of peroxide species with respect to almost perpendicular or slightly tilted superoxide species has recently been predicted. [16]

In this contribution, we present results on the O_2 adsorption and activation at reduced ceria nanoparticles of approximately the same size but selectively exposing (111) and (100) facets and show that surface orientation does matter. We employed in situ Raman spectroscopy in conjunction with state-of-the-art DFT calculations to detect peroxide, superoxide, and weakly bound dioxygen species and assign their adsorption sites, for the first time, employing a combined in situ Raman and DFT approach. While resolving previous literature ambiguities our approach provides a powerful basis for the description of O_2 adsorption and activation on other oxide powder catalysts.

Figure 1 depicts in situ Raman spectra (532 nm) of the synthesized ceria nanostructures (for details on the synthesis and characterization see Supporting Information) next to the corresponding transmission electron microcopy (TEM) images. The measured TEM layer spacings of the sheets/polyhedra of 0.31 nm (see Figs. 1A, B) and cubes of 0.27 nm (see Fig. 1C) compare

perfectly to the (111) and (200) reflexes of the cubic fluorite type lattice of ceria confirming the presence of (111) facets on the surface of sheets/polyhedra and (100) facets on that of the cubes. The sheets are rather uniform in size (12 nm) whereas polyhedra sizes range from 6 to 10 nm and those of the cubes from 11 to 60 nm. Specific surface areas were determined as 61 m^2/g for sheets, as 124 m^2/g for polyhedra, and as 51 m^2/g for cubes. The resulting crystal sizes are in line with those determined from TEM (see Table S1).

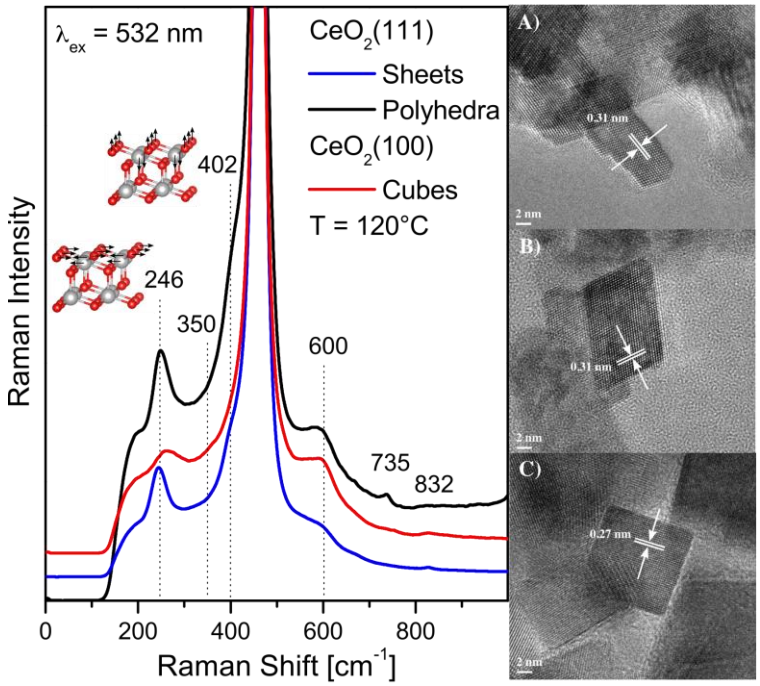

Figure 1. Left: In situ Raman spectra (532 nm) of ceria nanostructures. Spectra were taken in a constant gas flow of 25% O_2/Ar at a total flow rate of 100 ml/min and were normalized to the most intense F_{2g} band. Insets illustrate the longitudinal and transversal stretching mode of the CeO_2(111) surface. Right: Transmission electron microscopy (TEM) images of the ceria nanostructures: A) sheets, B) polyhedra, (C) cubes.

The in situ Raman spectra corroborate the results from electron microscopy. Recently, we have assigned the Raman features of polycrystalline ceria at 246 cm^{-1} and 402 cm^{-1} to longitudinal and transversal stretching modes of the CeO_2(111) surface on the basis of density functional perturbation theory calculations (see insets in Fig. 1). [32] Indeed the Raman spectra of sheets and polyhedra exhibit a band at 246 cm^{-1} and a shoulder at 402 cm^{-1}, whereas the intensity of the former is roughly doubled for the polyhedra as expected from the specific surface areas. Both features are absent in Raman spectra of ceria cubes. The smaller band at 264 cm^{-1} for the cubes is assigned to a 2TA overtone of bulk ceria [33] that is also present at sheets and polyhedra but largely covered by the corresponding longitudinal surface mode. [32] Generally, Raman spectra show differences between ceria sheet/polyhedra and nanocube surface modes and defect-related features at around 600 cm^{-1}.

To model the CeO_2(100) surface a checkerboard type reconstruction of the surface oxygen ions was assumed (for details on the DFT calculations see Supporting Information, see Fig. S5). [16] [34] [35] Note that other surface reconstructions have also been proposed. [36] [37] The vibrational analysis of the modeled surface reveals Raman active vibrations with frequencies of 331 cm^{-1} and 563 cm^{-1} (see Fig. S6). For ceria phonons calculated with the DFT(PBE)+U approach, [24] a scaling factor of 1.06 was found for the F_{2g} ceria mode, measured at 464 cm^{-1} and calculated at 437 cm^{-1}. Accordingly, the small shoulders at 350 cm^{-1} and 600 cm^{-1} observed in the Raman spectra of cubes (Fig. 1), can be assigned to the calculated vibrations of the (100) facet. The band at 735 cm^{-1} observed for polyhedra originates from residual nitrate impurities (see Fig. S1). Therefore, in the following we focused on sheets and cubes exhibiting comparable specific surface areas and selectively exposing CeO_2(111) and CeO_2(100) facets, respectively. The thermal stability of the

(100) and (111) surface facets was confirmed up to 120°C (see Supporting Information, see Fig. S2).

In Fig. 2 Raman spectra in the region 700-1700 cm^{-1} are shown highlighting the effect of the exposed facet orientation. Specifically, peroxide species are observed at both surfaces, but superoxide ones only at the (100) facet. Moreover, the peroxide intensities are higher on that surface and, as discussed in the following, the temperature-dependent behavior and the relative intensities of the peroxide features depend on the facet exposed. For the CeO_2(111) facet, the peroxide intensity shrinks at elevated temperatures (60°C and 120°C) in oxygen flow. In a reducing environment the intensity is larger compared to that in oxidizing environments and it is most intense upon exposure to CO/O_2 (cf. Fig. 2, bottom left, brown spectrum). We attribute the increased peroxide (and superoxide) intensity during/after CO/O_2 flow to the formation of surface oxygen vacancies due to removal of weakly bound molecularly adsorbed oxygen such as $O_2^{\delta-}$ species. From the spectrum in CO/O_2 it is apparent that the main peroxide feature at 832 cm^{-1} possesses a second component at 860 cm^{-1}. The peroxide adsorption behavior can be readily understood in the light of our recent DFT+U results [32] predicting two peroxide configurations with comparable O_2^{2-} adsorption energies at the $CeO_{2-x}(111)$ surface (cf. Table S2), namely, $E_{ads,O_2^{2-}} = -1.900$ eV (outer O leans toward a Ce^{4+}, O–O stretch at 900 cm^{-1}) and $E_{ads,O_2^{2-}} = -1.919$ eV (outer O leans toward a subsurface O atom, O–O stretch at 938 cm^{-1}; less intense), in line with previous experimental [20] [21] [22] and DFT+U [30] studies calculating a 20 meV barrier for transitions between them. Besides, a further blue shifted frequency (calculated at 973 cm^{-1}) was predicted for agglomerated peroxides (1 ML peroxides $E_{ads,O_2^{2-}} = -1.773$ eV), [29] and previously observed at polycrystalline ceria at low temperature. [18] This behavior shows that a blue shift of the peroxide mode can also be caused by agglomeration of peroxide molecules at the surface (coverage effect).

For the (111) facet, O_2^{2-} vibrations show a decline in intensity with increasing temperature without major changes in the 832 cm^{-1}/860 cm^{-1} intensity ratio. However, for the (100) facet, the intensity of the band at 832 cm^{-1} increases at 60°C and strongly decreases at 120°C, whereas the second component at 862 cm^{-1} is stable at 21°C and 60°C but increases at 120°C and after cooling to 21°C (see Fig. S3). Based on the known coverage effect of peroxides on the (111) facet discussed above and the prediction of the existence of only one type of stable peroxide species at the (100) surface, the existence of two peroxide species at the latter indicates an increased population of isolated peroxide molecules at 60°C (832 cm^{-1} band in Fig. 2) and the formation of stable O_2^{2-} aggregates at 120°C (862 cm^{-1} band in Fig. 2). Indeed, for the CeO_{2-x}(100) surface, DFT+U calculations reveal only one stable peroxide configuration for coverages up to 0.25 ML with the O_2^{2-} species lying flat as depicted in the bottom inset of Fig. 3, and a calculated adsorption energy of $E_{ads,O_2^{2-}} = -2.141$ eV as well as a O–O stretching vibration at 868 cm^{-1} for a $p(2\times2)$ structure (0.25 ML). Note that our result is in-line with that recently published by Yang *et al.* [16] Precisely, if we use their computational setup that includes dispersion interactions, we closely reproduced the reported data (Table S3). In the following, we will refer to results obtained using the same settings as in our previous study on the O_2^{2-}/CeO_{2-x}(111) system, [32] though pointing out that the inclusion of dispersion interactions has only a minor influence on the results (orange, dark blue, and gray dots in Figs. 3 and 4). At this point, we relate the lower intensity of the observed 832 cm^{-1} peak at the (111) surface as compared to that for the (100) to the lower binding energy of peroxide species at the former (cf. Tables S2 and S4). Figure 3 depicts the calculated peroxide stretching frequency as a function of coverage. The frequency shifts from 868 cm^{-1} for coverages ≤0.25 ML to 873 cm^{-1} for 0.5 ML coverage, whereas for a full monolayer, a blue shift to 907 cm^{-1} is observed together with a rearrangement of the peroxide molecule adopting a 14° angle with respect to the surface

plane (see Fig. S8 for all structures). By assigning the two regimes of low and highest peroxide coverage to the two experimentally observed bands at 832 cm^{-1} and 862 cm^{-1} and interpolating by a linear function, $\tilde{\nu}_{theo} = 1.30 \bullet \tilde{\nu}_{exp}$ -214 cm^{-1}, we are able to describe coverage effects. We note that exactly the same slope of 1.30 has been obtained for describing such effects at the CeO_2(111) surface. However, at the (100) facet only a single peroxide configuration for isolated peroxide molecules was found. [31] This finding highlights that comparable effects govern peroxide agglomeration and contribute to the O–O stretch frequencies at both ceria facets.

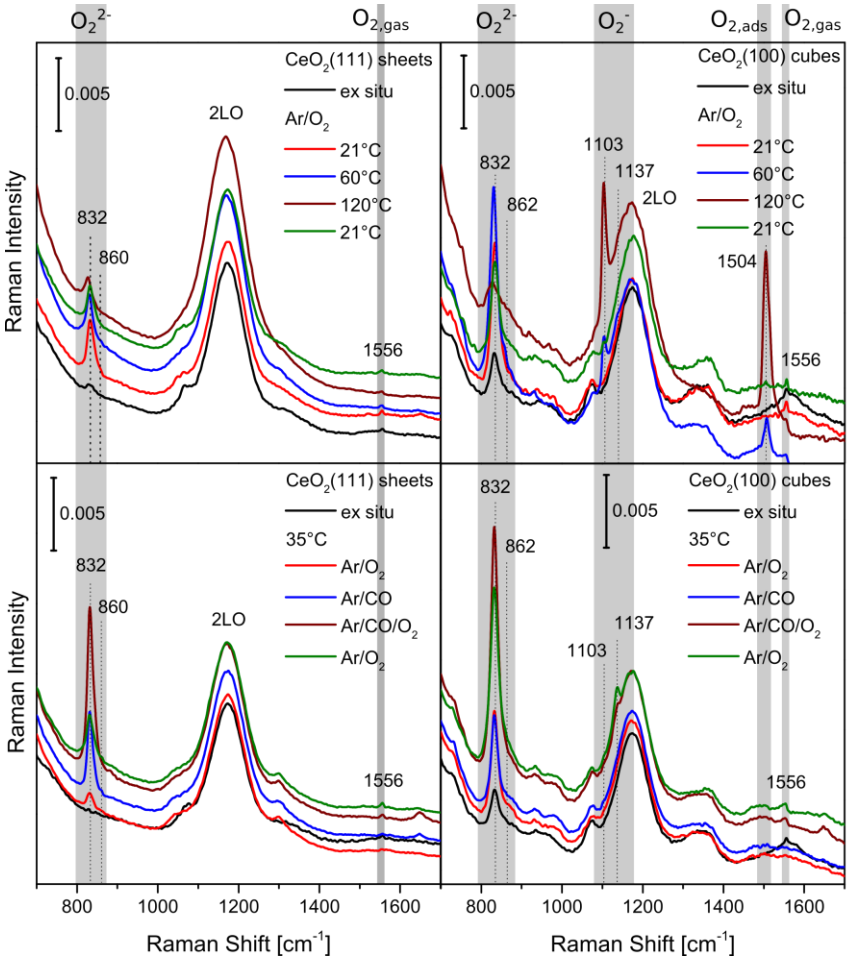

Figure 2. Spectral region of adsorbed oxygen species of in situ Raman spectra (532 nm) of CeO_2 sheets (left) and cubes (right) in 25%O_2/Ar flow at different temperatures (top) and during

oxidizing (25% O_2/Ar), reducing (2% CO/Ar), and reaction (2% CO/10% O_2/Ar) conditions at 35°C (bottom). During the temperature-dependent experiments the samples were first heated to the desired temperatures in 25% O_2/Ar flow by applying a heating ramp of 15°C/min and then held at each of those temperatures for about 60 min. Cooling from 120°C back to 21°C took place initially at 15°C/min and later at 5°C/min on average. Spectra were normalized to the F_{2g} band intensity. The omnipresent band at 1556 cm^{-1} is due to gas phase oxygen.

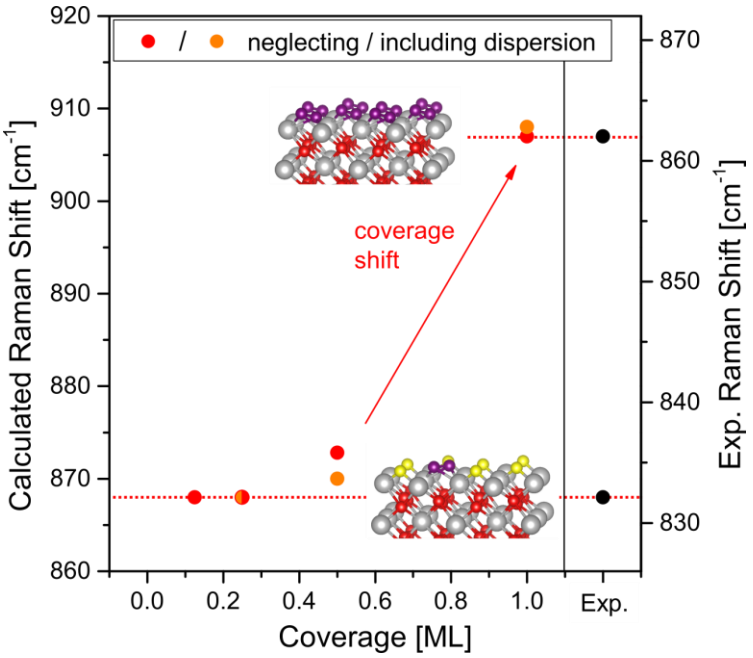

Figure 3. Calculated peroxide stretch frequency for $O_2^{2-}/CeO_{2-x}(100)$ structures as a function of coverage. The models depict the structures for 1 ML (top) and 0.125 ML (bottom) coverage. Red and orange circles refer to the absence and presence of dispersion interactions in the calculations, respectively. The experimental bands (indicated by black circles) at 832 and 862 cm^{-1} are correlated to the calculated bands at 868 and 907 cm^{-1}.

Figure 2 demonstrates that for $CeO_2(100)$ facets superoxide Raman bands are observed at 1103 cm^{-1} and at 1137 cm^{-1}, representing the first Raman report of such species at ceria nanocubes. In previous Raman studies on nanocubes superoxides were not observed probably due to the presence of impurities. [24] Recently, the existence of nearly upright superoxides at single crystal (100) surfaces has been reported using IR spectroscopy and DFT+U calculations. [16] However, we found that up to a coverage of 0.5 ML, only flat-lying superoxide species are stable. Structures showing an angle with respect to the surface plane are predicted to be transition state structures (see Tables S3, S4 and Figs. S9, S10). Moreover, we considered three different configurations for

the location of the Ce^{3+} cation, namely, nearest neighbor (NN) and next nearest neighbor (NNN) to the O_2^- species at the surface or NNN in the subsurface cerium layer (cf. Table S4, Fig. S9 and insets in Fig. 4). The configuration in which the Ce^{3+} is NN is predicted to be the most stable structure. For the example of the 0.125 ML coverage, the binding of a O_2^- species with a NN Ce^{3+} amounts to $E_{ads,O_2^-} = -1.344$ eV, whereas that with a NNN Ce^{3+} is by either 0.168 or 0.283 eV less stable, depending on whether the Ce^{3+} is at the surface or in the subsurface, respectively. For all other coverages considered, we refer to Table S2 and Fig. S9.

In Fig. 4 we show the calculated O–O vibrational frequency of the $O_2^-/CeO_{2-x}(100)$ structures as a function of coverage and configuration. At 0.125 ML coverage, the vibration is predicted at 1050 cm^{-1} for Ce^{3+} in NN position, whereas for Ce^{3+} in NNN positions at the surface and in the subsurface, lower frequencies of 1025 cm^{-1} and 1024 cm^{-1} are calculated, respectively. Clearly, the vibrational frequency depends on where the Ce^{3+} is located, giving rise to two distinct vibrational regimes. We attribute these values to the experimentally observed Raman bands at 1137 and 1103 cm^{-1}, i.e., the former is assigned to superoxides with Ce^{3+} in direct proximity, whereas the latter to superoxides with Ce^{3+} in NNN positions.

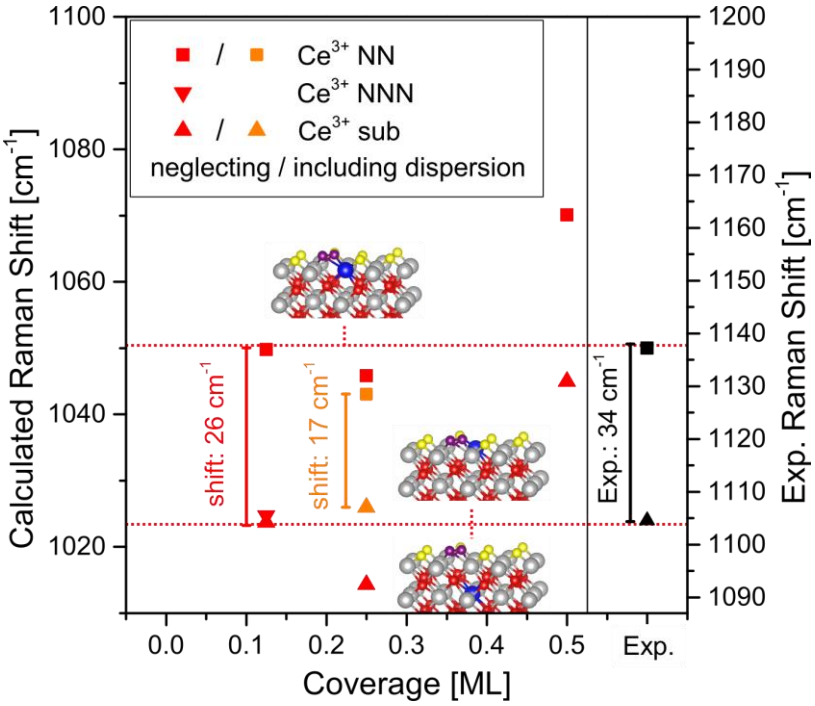

Figure 4. Calculated superoxide stretch frequency for $O_2^-/CeO_{2-x}(100)$ structures as a function of coverage and for different locations of the Ce^{3+} cation. The models depict the structures for 0.125 ML coverage, from top to bottom: Ce^{3+} in a NN position (squares), Ce^{3+} in a NNN position at the surface (triangle down), and Ce^{3+} in a NNN position in the subsurface (triangle up). Red and orange forms refer to the absence and presence of dispersion interactions in the calculations, respectively. Dashed lines indicate two distinct structural features, i.e., Ce^{3+} in direct proximity to superoxide (1050 cm^{-1}, experimental 1137 cm^{-1}) and in the second coordination sphere (1024 cm^{-1}, experimental 1103 cm^{-1}).

Summing up, for the $CeO_{2-x}(100)$ facets, we found that peroxide species are more stable than superoxide ones (cf. Table S4). Nonetheless, superoxides can form either due to an increase in temperature leading to a shift in the equilibrium between O_2^{2-} and O_2^- ($O_2^{\acute{o}-}$) species towards the

more weakly bound oxygen species, as indicated by the appearance of bands at 1103 cm^{-1} (O_2^-) and 1504 cm^{-1} (O_2^{6-}) or during / after CO/O_2 treatment at 35°C indicated by the band at 1137 cm^{-1} (see Fig. 2). This can be rationalized by a dynamic oxygen vacancy formation during CO oxidation and transfer of only one electron to molecular oxygen in the gas phase that initially adsorbs as a superoxide molecule. Certainly, this represents a metastable state since the transfer of a second electron would further stabilize the oxygen species as a flat-lying peroxide molecule. Treatment in Ar/O_2 flow after reaction-induced vacancy formation leads to additional oxygen adsorption as superoxide and thus an increase of the 1137 cm^{-1} band (see Fig. 2). Yet, the observation of a second superoxide species (1103 cm^{-1}, Fig. 2) with Ce^{3+} in a NNN position can be rationalized by the hopping of the excess electron to a NNN Ce ions at the surface or in subsurface Ce layers, which is known to be an activated process with an experimentally determined barrier of about 0.5 eV for bulk ceria, [38] and thus it is not expected to occur at too low temperatures, in-line with the experimental observations. Since the superoxide and most stable peroxide species are simultaneously observed, we conclude that the transformation of the former into the latter is kinetically hindered.

As mentioned above, in recent IR experiments on single crystal $CeO_2(111)$ surfaces at 80 K neither peroxide nor superoxide species were found. [16] This behavior has been attributed to the known preferred localization of oxygen vacancies in the subsurface, i.e., at sites not directly accessible by gas phase oxygen. [39 40 41] However, in contrast to single crystals, the here considered (111) truncated nanoparticles obviously possess surface and subsurface oxygen vacancies and peroxides species form at 35°C. Furthermore, in accordance with the behavior at the $CeO_2(111)$ single crystal surface, [16] but in contrast to previous Raman [20 21 22 24 42] and IR [25 26 27 43] results at polycrystalline surfaces, no superoxides ($\tilde{\nu} = 1123\text{-}1131\ cm^{-1}$) have been observed in our

experiments at the (111)-oriented facets due to the high instability of such species at ambient conditions.

Finally, at the (100) facets a band at 1504 cm^{-1} is observed at 60°C, which becomes very intense at 120°C. This is assigned to weakly bound dioxygen species ($O_2^{\delta-}$) at the unsaturated CeO_2(100) surface. We found that such species are very weakly adsorbed oxygen species (cf. Table S4) with a calculated O–O vibrational frequency within the 1544–1550 cm^{-1} range. In addition, in Figure 2, the omnipresent band at 1556 cm^{-1} is due to gas phase oxygen, whereas the weak feature at around 1080 cm^{-1} may tentatively be assigned to ozone species [44].

Summarizing, we have reported on the facet-dependent oxygen adsorption of ceria nanoparticles employing a combined in situ Raman and DFT approach for the first time. A strong variation in adsorption behavior has been found, that is facilitated for (100) facets, enabling identification of different kinds of di-oxygen species (O_2^{x-}, x = 0, δ, 1, 2) as well as two possible regimes for superoxide formation at (100) facets assigned to the distinct excess charge localization in either nearest or next nearest neighbor cationic position to the superoxide species on the basis of computational modeling and DFT calculations.

On one hand, our study transfers the knowledge of the importance of the surface crystallographic orientation of planar (single crystal) surfaces for the activation of oxygen molecules [16 17] to nanoparticle ceria that can be employed as working catalysts, helping bridging the materials gap between the idealized and real catalytic systems. On the other hand, it shows the potential of Raman spectroscopy for in situ characterization of adsorbed and activated oxygen species on oxide surfaces.

Supporting Information

The Supporting Information cover a detailed description of the experimental and computational procedures, in situ Raman spectra, as well as DFT results for CeO_2(111) and CeO_2(100).

Notes

The authors declare no competing financial interest.

Acknowledgements

C.S. gratefully acknowledges a scholarship by the Merck'sche Gesellschaft für Kunst und Wissenschaft e.V. M.V.G.P. acknowledges support by the MINECO-Spain (CTQ2015-78823-R). Calculations were conducted on the Lichtenberg high performance computer at the TU Darmstadt. Computer time provided by the Spanish Supercomputer Network (RES) is also acknowledged. Stefan Lauterbach and Hans-Joachim Kleebe (TU Damstadt) are gratefully acknowledged for TEM measurements.

References

1. Gandhi, H. S.; Graham, G. W.; McCabe, R. W. Automotive Exhaust Catalysis. *J. Catal.* **2003,** *216*, 433-442.
2. Gorte, R. J. Ceria in Catalysis: From Automotive Applications to the Water Gas Shift Reaction. *AlChE J.* **2010,** *56*, 1126-1135.
3. Zhou, K.; Wang, X.; Sun, X.; Peng, Q.; Li, Y. Enhanced Catalytic Activity of Ceria Nanorods from well-defined Reactive Crystal Planes. *J. Catal.* **2005,** *229*, 206-212.
4. Vilé, G.; Bridier, B.; Wichert, J.; Pérez-Ramírez, J. Ceria in Hydrogenation Catalysis: High Selectivity in the Conversion of Alkynes to Olefins. *Angew. Chem. Int. Ed.* **2012,** *51*, 8620-8623.
5. Schilling, C.; Hess, C. Real-Time Observation of the Defect Dynamics in Working Au/CeO_2 Catalysts by Combined Operando Raman/UV–Vis Spectroscopy. *J. Phys. Chem. C* **2018,** *122*, 2909-2917.
6. Carrasco, J.; López-Durán, D.; Liu, Z.; Duchoň, T.; Evans, J.; Senanayake, S. D.; Crumlin, E. J.; Matolín, V.; Rodríguez, J. A.; Ganduglia-Pirovano, M. V. In Situ and Theoretical Studies for the Dissociation of Water on an Active Ni/CeO_2 Catalyst: Importance of Strong Metal–Support Interactions for the Cleavage of O–H Bonds. *Angew. Chem. Int. Ed.* **2015,** *54*, 3917-3921.
7. Liu, Z.; Lustemberg, P.; Gutiérrez Ramón, A.; Carey John, J.; Palomino Robert, M.; Vorokhta, M.; Grinter David, C.; Ramírez Pedro, J.; Matolín, V.; Nolan, M. *et al.* In Situ Investigation of Methane Dry Reforming on Metal/Ceria(111) Surfaces: Metal–Support Interactions and C−H Bond Activation at Low Temperature. *Angew. Chem. Int. Ed.* **2017,** *56*, 13041-13046.
8. Park, S.; Vohs, J. M.; Gorte, R. J. Direct Oxidation of Hydrocarbons in a Solid-Oxide Fuel Cell. *Nature* **2000,** *404*, 265-267.
9. Trovarelli, A.; Fornasiero, P. (eds.) *Catalysis by Ceria and Related Materials*. Imperial College Press: London; 2013.
10. Fornasiero, P.; Cargnello, M. (eds.) *Morphological, Compositional, and Shape Control of Materials for Catalysis*. Studies in Surface Science and Catalysis, Vol. 177. Elsevier: Amsterdam; 2017.

11. Agarwal, S.; Zhu, X.; Hensen, E. J. M.; Mojet, B. L.; Lefferts, L. Surface-Dependence of Defect Chemistry of Nanostructured Ceria. *J. Phys. Chem. C* **2015,** *119*, 12423-12433.
12. Mai, H.-X.; Sun, L.-D.; Zhang, Y.-W.; Si, R.; Feng, W.; Zhang, H.-P.; Liu, H.-C.; Yan, C.-H. Shape-Selective Synthesis and Oxygen Storage Behavior of Ceria Nanopolyhedra, Nanorods, and Nanocubes. *J. Phys. Chem. B* **2005,** *109*, 24380-24385.
13. Zhang, J.; Kumagai, H.; Yamamura, K.; Ohara, S.; Takami, S.; Morikawa, A.; Shinjoh, H.; Kaneko, K.; Adschiri, T.; Suda, A. Extra-Low-Temperature Oxygen Storage Capacity of CeO_2 Nanocrystals with Cubic Facets. *Nano Lett.* **2011,** *11*, 361-364.
14. Trovarelli, A.; Llorca, J. Ceria Catalysts at Nanoscale: How Do Crystal Shapes Shape Catalysis? *ACS Catal.* **2017,** *7*, 4716-4735.
15. Wu, Z. L.; Li, M. J.; Overbury, S. H. On the Structure Dependence of CO Oxidation over CeO_2 Nanocrystals with Well-Defined Surface Planes. *J. Catal.* **2012,** *285*, 61-73.
16. Yang, C.; Yu, X.; Heißler, S.; Weidler, P. G.; Nefedov, A.; Wang, Y.; Wöll, C.; Kropp, T.; Paier, J.; Sauer, J. O_2 Activation on Ceria Catalysts - The Importance of Substrate Crystallographic Orientation. *Angew. Chem. Int. Ed.* **2017,** *56*, 16399-16404.
17. Esch, F.; Fabris, S.; Zhou, L.; Montini, T.; Africh, C.; Fornasiero, P.; Comelli, G.; Rosei, R. Electron Localization Determines Defect Formation on Ceria Substrates. *Science* **2005,** *309*, 752.
18. Yang, C.; Yu, Xu; Heißler, S.; Nefedov, A.; Colussi, S.; Llorca, J.; Trovarelli, A.; Wang, Y.; Wöll, C. Surface Faceting and Reconstruction of Ceria Nanoparticles. *Angew. Chem. Int. Ed.* **2017**, *56*, 375-379.
19. Datta, S.; Torrente-Murciano, L. Nanostructured Faceted Ceria as Oxidation Catalyst. *Curr. Op. Chem. Eng.* **2018**, *20*, 99–106
20. Pushkarev, V. V.; Kovalchuk, V. I.; d'Itri, J. L. Probing Defect Sites on the CeO_2 Surface with Dioxygen. *J. Phys. Chem. B* **2004,** *108*, 5341-5348.
21. Guzman, J.; Carrettin, S.; Corma, A. Spectroscopic Evidence for the Supply of Reactive Oxygen during CO Oxidation Catalyzed by Gold Supported on Nanocrystalline CeO_2. *J. Am. Chem. Soc.* **2005,** *127*, 3286-3287.
22. Choi, Y. M.; Abernathy, H.; Chen, H.-T.; Lin , M. C.; Liu, M. Characterization of O_2–CeO_2 Interactions Using In Situ Raman Spectroscopy and First-Principle Calculations. *ChemPhysChem* **2006,** *7*, 1957-1963.

23. Filtschew, A.; Hofmann, K.; Hess, C. Ceria and Its Defect Structure: New Insights from a Combined Spectroscopic Approach. *J. Phys. Chem. C* **2016**, *120*, 6694-6703.
24. Wu, Z. L.; Li, M. J.; Howe, J.; Meyer, H. M.; Overbury, S. H. Probing Defect Sites on CeO_2 Nanocrystals with Well-Defined Surface Planes by Raman Spectroscopy and O_2 Adsorption. *Langmuir* **2010,** *26*, 16595-16606.
25. Li, C.; Domen, K.; Maruya, K.; Onishi, T. Dioxygen Adsorption on Well-Outgassed and Partially Reduced Cerium Oxide studied by FT-IR. *J. Am. Chem. Soc.* **1989,** *111*, 7683-7687.
26. Huang, X.; Beck, M. J. Size-Dependent Appearance of Intrinsic O_x^q "Activated Oxygen" Molecules on Ceria Nanoparticles. *Chem. Mater.* **2015**, *27*, 5840-5844.
27. Wu, Z.; Cheng, Y.; Tao, F.; Daemen, L.; Foo, G. S.; Nguyen, L.; Zhang, X.; Beste, A.; Ramirez-Cuesta, A. J. Direct Neutron Spectroscopy Observation of Cerium Hydride Species on a Cerium Oxide Catalyst. *J. Am. Chem. Soc.* **2017**, *139*, 9121-9727.
28. Ganduglia-Pirovano, M. V.; Hofmann, A.; Sauer, J. Oxygen Vacancies in Transition Metal and Rare Earth Oxides: Current State of Understanding and Remaining Challenges. *Surf. Sci. Rep.* **2007,** *62*, 219-270.
29. Paier, J.; Penschke, C.; Sauer, J. Oxygen Defects and Surface Chemistry of Ceria: Quantum Chemical Studies Compared to Experiment. *Chem. Rev.* **2013,** *113*, 3949-3985.
30. Huang, M.; Fabris, S. Role of Surface Peroxo and Superoxo Species in the Low-Temperature Oxygen Buffering of Ceria: Density Functional Theory Calculations. *Phys. Rev. B: Condens. Matter* **2007,** *75*, 081404.
31. Zhao, Y.; Teng, B.-T.; Wen, X.-D.; Zhao, Y.; Chen, Q.-P.; Zhao, L.-H.; Luo, M.-F. Superoxide and Peroxide Species on CeO_2(111), and Their Oxidation Roles. *J. Phys. Chem. C* **2012,** *116*, 15986-15991.
32. Schilling, C.; Hofmann, A.; Hess, C.; Ganduglia-Pirovano, M. V. Raman Spectra of Polycrystalline CeO_2: A Density Functional Theory Study. *J. Phys. Chem. C* **2017,** *121*, 20834-20849.
33. Weber, W.; Hass, K.; McBride, J. Raman Study of CeO_2: Second-Order Scattering, Lattice Dynamics, and Particle-Size Effects. *Phys. Rev. B: Condens. Matter* **1993,** *48*, 178-185.
34. Kropp, T.; Paier, J. Activity versus Selectivity of the Methanol Oxidation at Ceria Surfaces: A Comparative First-Principles Study. *J. Phys. Chem. C* **2015,** *119*, 23021-23031.

35. Nolan, M. Healing of Oxygen Vacancies on Reduced Surfaces of Gold-Doped Ceria. *J. Chem. Phys.* **2009,** *130*, 144702.

36. Pan, Y.; Nilius, N.; Stiehler, C.; Freund, H. J.; Goniakowski, J.; Noguera, C. Ceria Nanocrystals Exposing Wide (100) Facets: Structure and Polarity Compensation. *Adv. Mater. Interf.* **2014,** *1*, 1400404.

37. Capdevila-Cortada, M.; López, N Entropic Contributions Enhance Polarity Compensation for CeO_2(100) Surfaces. *Nature Mater.* **2017**, *16*, 328-335.

38. Tuller, H. L.; Nowick, A. S., Small Polaron Electron Transport in Reduced CeO_2 Single Crystals. *J. Phys. Chem. Solids* **1977,** *38* (8), 859-867.

39. Murgida, G. E.; Ganduglia-Pirovano, M. V. Evidence for Subsurface Ordering of Oxygen Vacancies on the Reduced CeO_2(111) Surface Using Density-Functional and Statistical Calculations. *Phys. Rev. Lett.* **2013,** *110*, 246101.

40. Ganduglia-Pirovano, M. V.; Da Silva, J. L. F.; Sauer, J. Density-Functional Calculations of the Structure of Near-Surface Oxygen Vacancies and Electron Localization on CeO_2(111). *Phys. Rev. Lett.* **2009**, *102*, 026101.

41. Han, Z.-K.; Yang, Y.-Z.; Zhu, B.; Ganduglia-Pirovano, M. V.; Gao, Y. Reduced CeO_2(111) Ordered Phases as Bulk Terminations: Introducing the Structure of Ce_3O_5. *Phys. Rev. Mater.* **2018**, *2*, 035802.

42. Filtschew, A.; Stranz, D.; Hess, C. Mechanism of NO_2 Storage in Ceria Studied Using Combined In Situ Raman/FT-IR Spectroscopy. *Phys. Chem. Chem. Phys.* **2013,** *15*, 9066-9069.

43. Haneda, M.; Mizushima, T.; Kakuta, N. Behaviour of Oxygen Species Adsorbed on Al_2O_3-Supported Cerium Oxide Catalysts for Methane Oxidation. *J. Chem. Soc., Faraday Trans.* **1995,** *91*, 4459-4465.

44. Bulanin, K. M.; Lavalley, J. C.; Lamotte, J.; Mariey, L.; Tsyganenko, N. M.; Tsyganenko, A. A. Infrared Study of Ozone Adsorption on CeO_2, *J. Phys. Chem. B* **1998**, *102*, 6809-6816.